# Characterization of internal tide incoherence : Eulerian versus Lagrangian perspectives

Zoé Caspar-Cohen*, Aurélien Ponte

*Ifremer,Université de Brest, CNRS, IRD, Laboratoire d'Océanographie Physique et Spatiale (LOPS), IUEM,Brest,France*

Noé Lahaye

*Inria, IRMAR, campus universitaire de Beaulieu, Rennes, France*

Xavier Carton, Xiaolong Yu and Sylvie Le Gentil

*Ifremer,Université de Brest, CNRS,IRD, Laboratoire d'Océanographie Physique et Spatiale (LOPS), IUEM,Brest,France*

*Corresponding author*: Zoé Caspar-Cohen, zoe.caspar@ifremer.fr

ABSTRACT

The Lagrangian and Eulerian surface current signatures of a low-mode internal tide propagating through a turbulent balanced flow are compared in idealized numerical simulations. Lagrangian and Eulerian total (i.e. coherent plus incoherent) tidal amplitudes are found to be similar. Compared to Eulerian diagnostics, the Lagrangian tidal signal is more incoherent with comparable or smaller incoherence timescales and larger incoherent amplitudes. The larger level of incoherence in Lagrangian data is proposed to result from the deformation of Eulerian internal tide signal induced by drifter displacements. Based on the latter hypothesis, a theoretical model successfully predicts Lagrangian autocovariances by relating Lagrangian and Eulerian autocovariances and the properties of the internal tides and jet. These results have implications for the separation of balanced flow and internal tides signals in the sea level data collected by the future Surface Water and Ocean Topography (SWOT) satellite mission.

## 1. Introduction

The disentangling of internal tides and balanced flow is a key issue for incoming wide-swath altimetric missions such as the SWOT (Surface and Water and Ocean Topography, (Morrow et al. 2019)) and Guanlan (Chen et al. 2019). SWOT will in particular provide instantaneous 2D sea level maps, with an expected horizontal resolution of the order of 15–45 km (Wang et al. 2019). With this resolution, internal tides and mesoscale balanced flow will be captured, providing a unique opportunity to study both motions and their interactions. While both motions have distinct time scales, they can have similar length scales (order of tens to hundreds of kilometers) which makes their separation via spatial filtering difficult. The coarse temporal resolution of these instruments (20 day repeat time approximately for SWOT) will also prevent separation by temporal filtering. The resulting difficult disentanglement of internal tides and balanced flow in wide-swath altimetric data is expected to deteriorate the quality of surface velocity estimations via geostrophy (Chelton et al. 2019). Internal tides (or baroclinic tides) are internal waves generated by the barotropic tide when it passes over a topography (Garrett and Kunze 2007). They are initially phase-locked with the tidal forcing and would remain so if they were propagating in a quiescent environment. Such phase-locked internal tide field is commonly referred to as coherent or stationary. (To avoid any confusion with the concept of stationarity in the context of statistics, we shall use the term "coherent" throughout this paper.) However, as internal tides travel in a background stratification that varies in time (Buijsman et al. 2017), or pass through a turbulent jet (Ponte and Klein 2015; Dunphy et al. 2017; Savage et al. 2020), they are disturbed and progressively loose their coherence. The fraction of the internal tide that is no longer phase-locked with the tidal forcing and/or of not constant amplitude is the incoherent internal tide, and the mechanisms and typical timescales associated with this loss of coherency remains insufficiently constrained at present days. Internal tides can then be scattered (towards different scales or frequency), e.g. by the

corrugated topography, or dissipated close or far from the generation's site (Whalen et al. 2020; Savva and Vanneste 2018; Savage et al. 2020). A fraction of the internal tides energy (mainly high modes) dissipates close to their generation's location (Whalen et al. 2020) but a significant part travels in the open ocean over potentially great distances – up to thousands of kilometers – with a low-mode vertical structure (Zhao et al. 2016).

Several works used altimeter observations to study baroclinic tide including its incoherent component. Because of their limited temporal sampling compared to internal tides periods, satellite altimetric observations enables the identification of the internal tide signature that remains coherent over a couple of years (Ray and Zaron 2016; Zaron 2019). More recently, averaged amplitudes of non-coherent sea level signatures were also obtained (Zaron 2017; Nelson et al. 2019).

To overcome limitations of altimeter data, the use of the global drifter program (GDP) dataset has recently been considered (Zaron 2017, 2019). GDP drifter tracks are resolved temporally down to an hour with a horizontal positioning sufficiently accurate in order to capture the signatures of near-inertial waves (Elipot et al. 2010; Sykulski et al. 2016) and tidal motions (Elipot et al. 2016; Yu et al. 2019; Zaron and Elipot 2020). Assuming specific stochastic models for low-frequency and near-inertial motions, Sykulski et al. (2016) designed for example efficient statistical methods in order to fit models parameters to drifter velocity time series.

One of the challenges associated with the analysis and interpretation of Lagrangian data is the advection of a drifter by the flow. The data collected by a drifter as it is displaced by the flow may entangle Eulerian spatial and temporal variability and give a distorted perspective of variability as described in the Eulerian frame of reference. LaCasce (2008) reviewed conceptual frameworks that have been developed in order to tackle this issue (Lumpkin et al. 2002; Middleton 1985; Davis 1983, 1985). Two regimes are typically identified: fixed float and frozen turbulence. The prevalence of one regime over the other

is determined by the parameter $\alpha = T_E/T_a$, where $T_E$ is the Eulerian evolution timescale of the flow and $T_a$ is the time required for a drifter to travel the Eulerian characteristic spatial scale of the observed fluctuation. $T_a$ is given by $L/U$, with U the typical advection velocity and L the spatial scale of fluctuations. If $\alpha \ll 1$, the time required for the drifter to travel the length $L$ is greater than the timescale of the fluctuation, $T_E$. In this case, one can expect an agreement between the Lagrangian and Eulerian timescales. Conversely, if $\alpha \gg 1$, it takes a drifter a time smaller than $T_E$ to travel a distance $L$, causing a more rapid fluctuation in the Lagrangian perspective. We apply in these paper these ideas to the case of the case of internal tides interacting with a balanced flow.

Zaron and Elipot (2020) found a spectral broadening of barotropic tidal peaks in Lagrangian data compared to Eulerian ones, due to flow and/or tides spatial inhomogeneity. Such broadening is expected to complicate the extraction of internal tides properties (e.g. overall amplitudes, coherence/non-coherent fractions, incoherent timescales) from lagrangian drifter data, depending on the regions of the ocean and the associated dynamical regime. In order to improve our understanding of this issue, we quantify and compare in this study the internal tide amplitudes and incoherence timescales diagnosed in Eulerian and Lagrangian frames of reference in an idealized configuration.

We first present the numerical set-up used in this study as well as the statistical models and methods used to estimate internal tide amplitudes and decorrelation timescales. The results are shown in the second part for one simulation at first, and then for several simulations with varying balanced flow intensities. Lastly, we develop a theoretical model to predict Lagrangian autocovariance from Eulerian one and qualitatively validate it against our numerical simulations. The Discussion of the results and Conclusion complete the paper.

## 2. Numerical simulations and Lagrangian data

### *a. Numerical simulations*

We performed idealized numerical simulations of an internal tide crossing a balanced flow. The numerical model is the Coastal and Regional Ocean COmunity model, CROCO (CROCO and CROCOTOOLS are available at https://www.croco-ocean.org ) solving the hydrostatic primitive equations. Its configuration follows Ponte et al. (2017) with a zonally periodic rectangular numerical domain (1024 km x 3072 km). The Coriolis frequency follows the beta-plane approximation and is representative of mid-latitudes. A turbulent zonal balanced flow crosses the domain at its center along the meridional direction. Numerical simulations are initialized with a baroclinically unstable balanced flow. Relaxation of zonally averaged fields towards initial conditions(velocities, temperature, sea level) maintains the turbulence generated by the balanced flow destabilization. Simulations with different balanced flow strength are obtained by modulating the strength of the initial balanced flow or equivalently the latitudinal thermal gradient. After 500 days, relaxation of the zonal mean fields toward the initial balanced flow is ceased. The balanced flow has a mean velocity amplitude maximum around 1450km in the center of the balanced flow (Fig.1a, red line). The balanced flow amplitude decays over the observed period of time with a maximum around 0.6 m/s at the beginning and around 0.4 m/s at the end. The balanced flow velocity is computed by averaging each velocity component (u and v) over 2 days. The balanced flow is surfaced intensified (Fig. 1c) and its vertical structure essentially consists of the barotropic and first baroclinic modes. In the center area, the low-passed velocity indicates ~60% and ~40% of the kinetic energy are found in the barotropic and first baroclinic mode respectively.

A mode-1 internal tide is generated at $y = 400$ km with a semi-diurnal frequency (2 cpd). Its signature at the surface dominates the total velocity amplitude in the northern and southern areas (Fig.1a, green line compared to red line). The mode-1 wavelength is

approximately between 170 and 185 km in the south and between 160 and 180km in the north.

It is worth mentioning that the first baroclinic mode accounts for 98% of the the internal tide's vertically-integrated kinetic energy south and north of the balanced flow and around 90% in the balanced flow. The generation of internal tide higher modes after interaction with the balanced flow is thus negligible in our simulations. Sponge layers at the top and the bottom of the domain ($y < 300$ km and $y > 2700$ km) prevent reflections against top and bottom boundaries. Finally, about 8000 simulated near-surface drifters (referred to as drifters in the rest of this study) are also initialized at day 500 on a regular grid extending from 600 km to 2400 km and are advected online (Fig.1b).

Dunphy et al. (2017) reports, for the same numerical setup, on the nature of interactions between balanced flow and internal tide and, in particular, on the role played by the respective vertical structures of both processes. This works instead focuses on the distortions of the internal tide signal induced by displacements of surface drifters which explains why most of the attention is paid next on surface flow properties. Further discussion on the relative spatial structures of both processes for this more specific issue are found in section 5a.

*b. Lagrangian outputs overview*

In the central part of the domain, the balanced flow dominates drifter net motions with averaged displacements of about 300 km in the $x$-direction and 160 km in the $y$-direction over a 40 day time window (Fig. 2c). For comparison purposes the internal tide wavelength is of about 175km. Away from the balanced flow (Fig.2a and e), the net distance traveled in the y-direction by the selected drifters is of about 20–30 km – which is a fraction of an internal tide wavelength. Internal tides, on the other hand, generate smaller periodical displacements, of the order of 2–3 km.

Eulerian and Lagrangian meridional velocity time series exhibit significant differences, visually, in the balanced flow at both low and internal tide frequency (amplitude and phase) over a 40 day temporal window (Fig. 2d). Meridional velocity time series outside the balanced flow (Fig. 2b and f) exhibit smaller differences between both frames of reference. Modulations of internal tide fluctuations are faster in the north compared to the south in both Eulerian and Lagrangian time series. This discrepancy reflects the loss of coherence of the internal tide as it propagates northward and interacts with the balanced flow.

### *c. Methods : Estimation of Eulerian and Lagrangian amplitudes and timescales*

To quantify the loss of coherence of internal tides and the differences and similarities between Eulerian and Lagrangian diagnostics, we estimate amplitude and decorrelation/incoherence time scales associated with the balanced flow and internal tides and compare the results in different parts of the domain.

#### 1) Autocorrelation models

For both the Eulerian and Lagrangian signals, we assume that a time dependent velocity component $v$ may be written as the sum of an internal tide part, $\widetilde{v}$, and a balanced (or jet) part, $\overline{v}$:

$$v = \widetilde{v} + \overline{v} \tag{1}$$

where actual spatial and temporal dependencies have been omitted. Note that an alternative would be to use a complex velocity, $w = u + iv$ instead of individual components (zonal or meridional) (Sykulski et al. 2016). This choice is justified when dealing with polarized motions such as near-inertial waves but is less relevant for internal tides. We considered that this is not needed in our case and would be more suited for more realistic

configurations including inertial waves (Sykulski et al. 2016).

We assume the internal tide velocity time series is described by :

$$\widetilde{v}(t) = \mathfrak{R}\left[\widetilde{v}_e(t)e^{i\omega t}\right] \text{ with } \mathfrak{R} \text{ the real part} \tag{2}$$

where $\widetilde{v}_e$ is the complex-valued amplitude of the tidal oscillations of the tides and depends slowly on time, thus capturing the incoherence of the tide, and, where $\omega/2\pi$ is the frequency of the internal tide.

The internal tide signal can be decomposed into coherent and incoherent contributions. The coherent part is defined with a coherent temporal averaging operator (i.e. a temporal average with fixed phased with respect to $\omega$ frequency oscillations) :

$$\widetilde{v}_{coh} = \langle\widetilde{v}\rangle_c, \tag{3}$$

$$= \mathfrak{R}\left[\langle\widetilde{v}_e\rangle e^{i\omega t}\right] \tag{4}$$

where $\langle\cdot\rangle$ is a time averaging operator.

Hence the incoherent part, defined as the total velocity minus the coherent part :

$$\widetilde{v}_{inc} = \widetilde{v} - \langle\widetilde{v}\rangle, \tag{5}$$

$$= \mathfrak{R}\left[(\widetilde{v}_e - \langle\widetilde{v}_e\rangle_c)e^{i\omega t}\right] \tag{6}$$

Assuming internal tide velocities and jet velocities are uncorrelated, the total autocovariance, C, equals to the sum of the autocovariances of $\widetilde{v}$ and $\overline{v}$ :

$$C(\tau) = \langle v(t)v(t+\tau)\rangle = \widetilde{C}(\tau) + \overline{C}(\tau), \tag{7}$$

There is no report in the literature nor clear physical expectations for the shape of incoherent signal complex envelopes. A heuristic choice is thus made here by assuming the envelope of the incoherent signal is an exponentially decaying function of time lag, with a decay timescale, $\widetilde{T}$, which will be referred to as the incoherence timescale. The

tide autocovariance is expressed as:

$$\widetilde{C}(\tau) = \left[\widetilde{V}_{coh}^2 + \widetilde{V}_{inc}^2 e^{-\tau/\widetilde{T}}\right] \times cos(\omega\tau) \tag{8}$$

where capital letters are constants.

This model bears some resemblance with the autocorrelation derived by Sykulski et al. (2016). We stress however that the resemblance is fortuitous as the derivation of Sykulski et al. (2016) is not expected to hold for internal tides whose generation mechanisms and dynamics differ substantially from that of near-inertial waves which would not justify the use of the same model a priori.

The balanced velocity autocovariance is assumed to have the simple form :

$$\overline{C}(\tau) = \overline{V}^2 e^{-\tau/\overline{T}} \tag{9}$$

where $\overline{T}$ is the decorrelation timescale. An alternative model was proposed by Veneziani et al. (2004), introducing a term of balanced flow oscillation, $\cos(\Omega\tau)$, which accounts for eddies and meanders. The model does improve the visual agreement between meridional autocorrelations and their fit in the center of the domain but does not affect estimates of internal tide properties which are the focus of this study. We thus opted for the simpler form Eq.9.

The total autocovariance is finally given by:

$$C(\tau) = \widetilde{C}(\tau) + \overline{C}(\tau) = \left[\widetilde{V}_{coh}^2 + \widetilde{V}_{inc}^2 e^{-\tau/\widetilde{T}}\right] \times cos(\omega\tau) + \overline{V}^2 e^{-\tau/\overline{T}} \tag{10}$$

## 2) Autocorrelations and parameters estimation

For each drifter's trajectory the velocity time series is split into segments of length $T_w$, overlapping each other by 50%. A time window of 40 day is chosen. This value is the result of the following compromise: time windows used for the computation of Lagrangian individual autocovariances has to be short enough for the result to be typical of a specific area, while being long enough to capture potentially long decorrelation

timescales. Eulerian mean velocities, averaged in time and zonal direction is interpolated on drifters trajectories and removed. No significant impacts of this removal were observed on the results for the tidal signal. Indiviudal autocovariances are then computed over each segment and averaged within 50 km wide meridional bins. Each autocovariance segment is attributed to a bin depending on the mean position over the period T. We did not find a significant sensitivity of our results to the length of the window. The Eulerian individual autocovariance is computed at each grid point using the same time windows and bin-averaged meridionally as for the Lagrangian autocovariance. Averaged autocovariances are then divided by the averaged autocovariance at time lag zero to obtain the averaged autocorrelation.

The heuristic model, developed in Section 2c1, is fitted to averaged autocovariances which provides estimates for parameters $\widetilde{T}$, $\widetilde{V}_{coh}$,$\widetilde{V}_{inc}$, $\overline{T}$ and $\overline{V}$ to find the best fit. The fit is done using a non linear least square regression (Jones et al. 2001–). Lower bounds are fixed to zero for amplitudes and, one and two days for $\widetilde{T}$ and $\overline{T}$ respectively. Confidence intervals are computed using a bootstrap method (Efron 1981). Within each bin, individual autocovariances are randomly resampled one hundred times (with replacement). Each resampled dataset leads to an averaged autocovariance and amplitudes and timescales parameters estimates using the fit described previously. 95% confidence intervals are derived from the distribution of the parameter estimates.

## 3. Signatures of internal tides and balanced flow in Eulerian and Lagrangian perspective

### *a. Velocity autocorrelations*

Lagrangian and Eulerian velocity autocorrelations (resp. Fig. 3 a and b; function of time lag and y) highlight three regimes that coincides with the southern ($y$ <1000km), central

(1000km< $y$ <1800km), and, northern ($y$ >1800km) parts of the numerical domain and correspond to typical drifter trajectories shown in Fig. 2a, c and e. Autocorrelation at these latitudes of interest are further shown in Fig. 4.

In the northern and southern parts of the numerical domain, semi-diurnal oscillations associated with internal tides, stand out on both Eulerian and Lagrangian autocorrelations. In these areas, the signal seems to be dominated by internal tides with no signature of the balanced flow visually. No decay of oscillations amplitudes with time lag are visible in the south —especially in the Eulerian perspective (see Fig. 4f)— indicating that internal tides are nearly coherent there. A mild decay of these oscillations is observed in the north, on the other hand, and indicates internal tides are partially incoherent there. There are no significant visual differences between Lagrangian and Eulerian autocorrelations in the northern and southern areas.

Conversely, the central area exhibits a decay – especially in the Lagrangian perspective – of the tidal oscillations combined to a slower general decay associated with the slower balanced motion. As observed in drifters trajectories and velocity time series (Fig. 2, panels c and d), this is the area where drifters are most significantly displaced by the balanced flow and where Lagrangian and Eulerian time series differ substantially. Semi-diurnal oscillations of the Lagrangian autocorrelation are not visible after lags of about 5 days (Fig. 3a and Fig. 4c) while they are observed after 20 days on the Eulerian autocorrelation (Fig. 3b and Fig. 4d). The decorrelation of the balanced motion is also faster in Lagrangian autocorrelation compared to Eulerian one, and exhibits a negative lobe around $\tau \sim 4$ days which we attribute to the meridionally oscillating trajectories of drifters caught in the balanced flow. The faster decay of the low-frequency signature on Lagrangian autocorrelations is attributed to the projection of spatial variability into temporal one along drifter trajectories (Lumpkin et al. 2002; LaCasce 2008).

*b. Estimates of velocity amplitudes and decorrelation timescales*

Eulerian meridional profiles of incoherence timescales and coherent and incoherent tide amplitudes (red lines Fig.5a, c and d) obtained after fitting averaged autocovariances onto Eq.10 translate a loss of the coherence of internal tides during the crossing of the balanced flow. In the south, the tidal signal is essentially coherent with Eulerian coherent amplitudes that are larger than incoherent ones ($\sim 0.06\,\mathrm{m\,s^{-1}}$ versus $\sim 0.01\,\mathrm{m\,s^{-1}}$; see Fig. 5c) and a flat envelope of autocorrelations oscillations (Fig. 4f).

In the center of the numerical domain, the internal tide propagation is perturbed by the balanced flow and results in a loss of coherence with larger Eulerian incoherent to coherent amplitude ratios. This trend culminates in the northern part of the domain with incoherent amplitudes up to $\sim 0.08\,\mathrm{m\,s^{-1}}$ and coherent amplitudes of about $\sim 0.05\,\mathrm{m\,s^{-1}}$. Note that the total (coherent+incoherent) tidal amplitude increases northward (more clearly seen on Fig. 6)e. This increase is caused by variations of the Coriolis frequency and of the stratification. Furthermore, a northwards surface intensification of the vertical mode structure requires an increase of the surface amplitude for a given vertically integrated energy flux. All together, these mechanisms result in a northward increase of the surface coherent and incoherent amplitude.

Incoherent timescales exhibit values of about 5 days in the south and increases northward to reach values comprised between 10 and 20 days. We note that the envelope of the Eulerian tidal oscillations in the north (blue lines Fig. 4b) does reach a plateau, consistent with a remaining coherent component and justifying the form of the fit for the motions we use (eq. 8).

Lagrangian parameters present a significantly different picture compared to the Eulerian one as suggested by drifter trajectories (Fig. 2 a, c and e) and autocorrelations (Fig. 3). In the south, the envelope of the Lagrangian autocorrelation (Fig. 4 e) decays faster than the Eulerian one. Lagrangian incoherent and coherent amplitudes (red lines on Fig. 5c

and d) present similar values (~0.03 $m\,s^{-1}$ and ~0.04 $m\,s^{-1}$ respectively). Incoherent timescales (Fig. 5a) remain between 10 and 20 days. In the center, incoherent amplitudes largely dominate and reach values of about ~0.08 $m\,s^{-1}$ against ~0.01 $m\,s^{-1}$ for coherent amplitudes. Incoherent timescales decrease sharply in the same area down to1 day in its center. The larger level of incoherence of internal tide signature on Lagrangian velocities compared to Eulerian one is coined "apparent incoherence" and attributed to the distortion of the Eulerian signal by balanced motions which is largest in the center area. In the north, such apparent incoherence diminishes and Lagrangian autocorrelations and parameters are comparable to Eulerian ones (Fig. 4 a and b, Fig. 5a,c and d).

As expected, balanced motions amplitudes diagnosed from autocorrelations parametric fit are maximum in the central area where the balanced flow resides (Fig. 5e). The Lagrangian balanced motion decorrelation timescales (Fig. 5b) reach the lowest boundary (~2 days) in the central area. The Eulerian decorrelation timescales are larger, ≤10 days. It corresponds to the area of high balanced amplitude (Fig. 5e). It also coincides with the area of low Lagrangian incoherence timescales which supports an apparent incoherence in Lagrangian diagnostics dominant in this part.

### *c. Sensitivity to the balanced flow EKE*

The sensitivity of internal tide Lagrangian/Eulerian properties to the balanced flow EKE is investigated with five numerical simulations of increasing balanced flow strength. The meridional distributions of velocity amplitudes (Figure 6b) indicates a two-fold increase across simulations (Fig.6b).

The internal tide total velocity amplitude, defined by $\sqrt{\widetilde{V}_{coh}^2 + \widetilde{V}_{inc}^2}$, increases northwards (Fig.6e), as explained in section 3b. This increase is more pronounced for larger balanced flow strength, as expected from the larger change of stratification, and is of similar magnitude in both Eulerian and Lagrangian perspectives.

Starting with the two most energetic simulations, $S_3$ and $S_4$, both Eulerian and Lagrangian diagnostics show a loss of coherence of internal tides that occurs when internal tides cross the balanced flow. In the south area, the incoherent Eulerian tidal amplitude is smaller than the coherent one by a factor 4 which indicates the internal tide is essentially there (dashed lines in Fig. 6c and d). Lagrangian coherent and incoherent amplitudes are comparable, on the other hand, which indicates some apparent incoherence. In the center area, Eulerian and Lagrangian incoherent amplitudes increase while Lagrangian coherent amplitude drops sharply to zero. Lagrangian incoherent timescales (Fig. 6a) reach minimal values ($\leq$5days) while Eulerian ones remain around or above 5 days in all simulations. The width of this area of apparent incoherence is clearly identified from Lagrangian incoherent timescales (Fig. 6a) and is consistent with the increase of the strength of the balanced flow (Fig. 6b). In the northern area, both simulations exhibit comparable Eulerian and Lagrangian incoherent amplitudes and timescales, i.e. there is little apparent incoherence.

In the intermediate case, $S_2$, a sharp decrease of Lagrangian coherent amplitude and incoherence timescales identifies apparent incoherence in the center area similarly to $S_3$ and $S_4$. However we find discrepancies in the Eulerian frame of reference. The Eulerian coherent amplitude drops sharply to 0 in the north while the incoherent timescale increases towards values between 30 and 40 days. This might be caused by a inconsistency of the fit in the north because the tidal oscillations do not reach a plateau in the 40 days time window.

Unlike $S_3$ and $S4$, the two least energetic simulations, $S_0$ and $S_1$, show a weak loss of coherence in Eulerian perspective as coherent amplitudes exceeds incoherent ones at all meridional positions. Lagrangian coherent amplitude drops sharply to zero in the balanced flow while the incoherent amplitude one exhibits a bump and timescales drop to 1 day.

This indicates that Lagrangian apparent incoherence is effective even in weakly energetic simulations.

## 4. Lagrangian model for autocovariance and comparison to observed autocovariance

### *a. Theoretical expectation for the Lagrangian autocorrelation*

A theoretical model is developed next in order to predict Lagrangian velocity autocovariances based on Eulerian ones along with flow parameters. The model effectively represents distortions, in the Lagrangian frame of reference, of Eulerian tidal fluctuations induced by drifters displacements associated with the balanced flow.

We then validate this model based on the Eulerian and Lagrangian autocovariance presented in previous sections.

We assume that the tidal signal is a modulated monochromatic wave propagating in a single direction (say $x$) and characterized by a frequency $\omega$ and wavenumber $k$:

$$\tilde{v}(x,t) = \mathfrak{R}\left\{\widetilde{v}_e(x,t)e^{i(\omega t - kx)}\right\}, \tag{11}$$

where $\tilde{v}_e$ is the complex amplitude, which varies slowly both in time and space. Let's consider a parcel traveling with the flow with trajectory $X(t)$. The autocovariance of $\tilde{v}$ as measured along the parcel trajectory is given by:

$$\widetilde{C}_L(\tau) = \langle \tilde{v}(t+\tau)\tilde{v}(t)\rangle, \tag{12}$$

$$= \frac{1}{2}\mathfrak{R}\left\{\left\langle \widetilde{v}_e\left[X(t+\tau),t+\tau\right]\widetilde{v}_e^*\left[X(t),t\right]e^{i\left[\omega\tau - k(X(t+\tau)-X(t))\right]}\right\rangle\right\}, \tag{13}$$

$$= \frac{1}{2}\mathfrak{R}\left\{e^{i\omega\tau}\times\left\langle \widetilde{v}_e\left[X(t+\tau),t+\tau\right]\widetilde{v}_e^*\left[X(t),t\right]e^{-ik\delta X(t,\tau)}\right\rangle\right\}, \tag{14}$$

where we assume that oscillation terms ($\propto e^{\pm 2i\omega t}$) are smoothed out by the averaging procedure and we have introduced the displacement $\delta X(t,\tau) = X(t+\tau) - X(t)$.

We assume here that the internal tide is not transported by the balanced surface flow which is reasonable for low mode internal tides as further discussed in section 5a. In such

case, the amplitude of the tide and the displacement are presumably uncorrelated:

$$\widetilde{C}_L(\tau) = \frac{1}{2}\Re\left\{e^{i\omega\tau} \times \left\langle \widetilde{v}_e\big[X(t+\tau),t+\tau\big]\widetilde{v}_e^*\big[X(t),t\big]\right\rangle \times \left\langle e^{-ik\delta X(t,\tau)}\right\rangle\right\}, \tag{15}$$

The second term in the product of (15) right hand-side combines both the spatial and temporal variability of the Eulerian tidal envelope in general. As further discussed in sect. 4b, horizontal displacements after time intervals comparable to a incoherent time scale can be expected to be smaller than the length scale of the complex amplitude of the tide, which leads to:

$$\left\langle \widetilde{v}_e\big[X(t+\tau),t+\tau\big]\widetilde{v}_e^*\big[X(t),t\big]\right\rangle \approx \widetilde{C}_e(\tau), \tag{16}$$

where $\widetilde{C}_e(\tau)$ is the fixed point (i.e. zero spatial lag) autocovariance of the tidal amplitude.

The displacement may be decomposed into a wave high frequency contribution and a lower frequency component that may be associated with an independent flow and/or wave motions themselves via second order effects (Wagner and Young 2015). The former contribution is time periodic with frequency $\omega$ and a bounded amplitude equal to the wave excursion ($\widetilde{V}/\omega$ where $\widetilde{V}$ is the amplitude of the wave velocity) which is small compared to $1/k$.

The low frequency displacement is likely to continuously grow on the other hand and produces a displacement that ultimately dominates in the exponential of (15) right hand-side third term, even for flow amplitudes smaller than tidal ones. We will thus ignore tide displacements in the latter exponential. To proceed further, we assume that the balanced flow is a stationary Gaussian process, with rms amplitude $\bar{V}$ (over one direction) and exponential decorrelation in time with typical time scale $\bar{T}$ – consistently with the model (9).

Such model – sometimes referred as an unbiased correlated velocity model in the literature (Gurarie et al. 2017) – corresponds to the time-homogeneous Ornstein-Uhlenbeck

process. The displacement $\delta X(t,\tau)$ is also a Gaussian process with null mean and variance given by (Pope 2015, Chap. 12):

$$\sigma^2(\tau) \equiv \langle \delta X(t,\tau)^2 \rangle = 2\bar{T}^2\bar{V}^2 \left[ \tau/\bar{T} - \left(1 - e^{-\tau/\bar{T}}\right) \right]. \tag{17}$$

Note that the variance of the displacement admits two asymptotic regimes : $\sigma^2(\tau) \to \bar{V}^2\tau^2$ for $\tau \ll \bar{T}$, and $\sigma^2(\tau) \to 2\bar{V}^2\bar{T}\tau$ for $\tau \gg \bar{T}$. The third term in the right hand side of eq. (15) may then be computed :

$$\left\langle e^{-ik\delta X(t,\tau)} \right\rangle = \int_{-\infty}^{\infty} \cos(k\delta X) p(\delta X) d\delta X, \tag{18}$$

$$= \int_{-\infty}^{\infty} \cos(k\delta X) \frac{e^{-\delta X^2/(2\sigma^2)}}{\sigma\sqrt{2\pi}} d\delta X \tag{19}$$

$$= e^{-\sigma^2 k^2/2} = \exp\left( -k^2\bar{V}^2\bar{T}^2 \left[ \tau/\bar{T} - (1 - e^{-\tau/\bar{T}}) \right] \right) \tag{20}$$

Combining (16) with (20) into (15) leads to the following expression for the autocovariance of internal tide in the Lagrangian frame of reference:

$$\widetilde{C}_L(\tau) = \widetilde{C}_e(\tau)\cos(\omega\tau) e^{-\sigma^2(\tau)k^2/2} \tag{21}$$

$$= \widetilde{C}_E(\tau) e^{-\sigma^2(\tau)k^2/2}, \tag{22}$$

which becomes with the heuristic model of Eulerian tidal autocovariance $\widetilde{C}_E$ (8):

$$\widetilde{C}_L(\tau) = \cos(\omega\tau) \left( \tilde{V}_{coh}^2 + \tilde{V}_{inc}^2 \exp(-\tau/\tilde{T}_E) \right) e^{-\sigma^2(\tau)k^2/2} \tag{23}$$

The Lagrangian autocorrelation (22) and (23) have no coherent part and decay as fast or faster than the Eulerian autocorrelation because of the last term on the right hand-side of both equations. This larger incoherence in the Lagrangian frame of reference embodies the "apparent" incoherence. Its origin is purely kinematic and associated with drifter displacements relative to tidal phase patterns as indicated by the origin of this term in (15).

The parameter $k\sigma(\tau)$ delimits two distinct regimes:

- Weak advection, $k\sigma(\tau) \ll 1$ : The signature of the tidal signal in the Lagrangian frame of reference matches the Eulerian one: $\widetilde{C}_L(\tau) \sim \widetilde{C}_E(\tau)$. Lagrangian coherent and non-coherent contributions directly reflect Eulerian ones.

- Strong advection, $k\sigma(\tau) \gg 1$ : Lagrangian and Eulerian autocorrelations differ substantially. The parameter $k\bar{V}\bar{T}$ controls the form of the Lagrangian tidal envelope. For $k\bar{V}\bar{T} \gg 1$, the exponential decay of the Lagrangian autocorrelation scales is quadratic in $\tau$ with decay time scale $1/k\bar{V}$: $\widetilde{C}_L(\tau) \sim \tilde{V}^2_{coh}\cos(\omega\tau) \times e^{-k^2\bar{V}^2\tau^2}$. For $k\bar{V}\bar{T} \ll 1$, the balanced flow decorrelation induces a linear exponential decay with decay time scale $1/k^2\bar{V}^2\bar{T}$: $\widetilde{C}_L(\tau) \sim \tilde{V}^2_{coh}\cos(\omega\tau) \times e^{-k^2\bar{V}^2\bar{T}\tau}$.

These theoretical predictions are in qualitative agreement with the observed decrease of Lagrangian coherent amplitude and incoherent time scales in the central area (Fig. 5 and 6 (a) and (d)).

*b. Comparison of observed autocovariances and predicted Lagrangian ones*

Observed Lagrangian internal tide autocorrelation envelopes (Fig. 7 middle column) are assembled from Lagrangian averaged autocovariance fitted parameters and Eq.8 (with the cosine term omitted and normalization by the value at lag 0). These envelopes are compared to predicted Lagrangian envelopes (Fig. 7 right column) estimated from observed Eulerian autocovariances (assembled similarly as Lagrangian ones and shown on Fig. 7 left column) and Eq. (22)

Observed Eulerian autocorrelation envelopes exhibit decay rates that are increasingly faster in the northwards direction for all three simulations considered ($S_0$, $S_2$ and $S_4$; shown in Fig. 7, top, middle and bottom rows respectively). This reflects the loss of coherence of the internal tide as it propagates northwards.

Observed Lagrangian autocorrelation envelopes have markedly different structure with a well-defined central area characterized by a rapid (couple of days timescale) fall-off

compared to Eulerian envelopes. The width of this area of strong apparent incoherence is increasing with the balanced flow strength. Outside of this area, the south and north autocorrelation decay are slower and hence closer to Eulerian ones with a more rapid decay in the north compared to the south. Predicted Lagrangian envelopes reproduce the rapid envelope fall-off in the center, the north/south contrast, as well as the sensitivity of the envelopes to balanced flow strength. We conclude the model proposed in order to relate Eulerian and Lagrangian tidal autocovariances is thus consistent with observations.

According to Eq.(22), Lagrangian incoherence can be governed either by Eulerian incoherence, or by the distortion of tidal signals induced by drifter displacements (i.e. apparent incoherence). The theoretical model indicates that the three following parameters provide the information necessary to interpret the nature of the Lagrangian incoherence: the ratio of Eulerian incoherent to coherent amplitude $\widetilde{V}_{inc}/\widetilde{V}_{coh}$ (Fig. 8a); the Lagrangian to Eulerian incoherent timescales $r_E = \widetilde{T}_L/\widetilde{T}_E$ (Fig. 8b); and $r_{a,inc} = k^2\sigma^2(\widetilde{T}_L)$ (Fig. 8c) which represents the apparent incoherence. If the model is exact and parameters are correctly estimated, at least one of the last two parameters should be about unity. These parameters are leveraged next in order to determine the regimes encountered in the numerical simulations and strengthen our interpretations.

In the southern area, the ratio of Eulerian incoherent to coherent amplitudes (Fig. 8a) is smaller than unity for all simulations : internal tides are coherent in the Eulerian frame of reference. The moderate values of the apparent incoherence parameter ($0.2 < r_{a,inc} < 0.4$) suggest float displacement do induce distortions of tidal signals and apparent incoherence. We speculate the values $r_{a,inc}$ are not closer to unity because of the inappropriate form of the decay employed in the fit (e.g. linear exponential decay vs quadratic), a point which is further discussed in section 4b.

In the central area, the ratio of Eulerian incoherent to coherent amplitudes increases but remains moderate (i.e. <1). The apparent incoherence parameter is maximum with values

up to unity. This coincides with values of $r_E$ smaller than 0.3 which equivalently states that the Lagrangian incoherence timescale is a fraction of the Eulerian one. This regime is one of strong apparent incoherence.

In the north, the ratio of Eulerian incoherent to coherent amplitudes is larger than one for $S_2$, $S_3$ and $S_4$, i.e. the tide is predominantly incoherent in the Eulerian frame of reference. For least energetic simulations ($S_0$ and $S_1$), the tide is predominantly coherent but with some incoherent contribution. The apparent incoherence term exhibits moderate to small values while the ratio $r_E$ is close to unity. We interpret this situation has one where the both Eulerian incoherence and apparent incoherence both contribute to the observed Lagrangian incoherence.

## 5. Discussion

*a. On the nature of internal tide propagation in the presence of a background flow*

The assumption of no transport of the internal tide by the surface flow used to derive (15) is now discussed. Low mode internal tides have by definition large vertical scales – similar to that of the background flow. Advection by the balanced flow is of particular importance for discussing the Eulerian/Lagrangian distortion, even though it does not fully capture the interaction between the balanced flow and the internal tide (Dunphy et al. 2017; Savage et al. 2020). A vertical mode expansion of equations of motions linearized around the balanced background flow shows that advection of the internal tide mode is driven by a non-trivial weighted average of the background flow. This effective advection is expressed as $H^{-1}\int_{-H}^{0}\phi_n^2\mathbf{U}dz$ (Kelly and Lermusiaux 2016), where $\phi_n$ is the standard pressure mode for an internal tide with vertical mode number $n$ and $\mathbf{U}$ is the balanced flow (see also Duda et al. 2018, for a more technical approach). Thus, for a surface intensified background flow, the flow advecting the drifter (at the surface) and the one advecting the

internal tide mode is different, explaining why the Lagrangian observer renders a distorted view of the internal tide signal.

For the simulation with moderate jet intensity S2, for instance, the mode 1 effective advection velocity (computed, but not shown) is of order $0.2\,\mathrm{m\,s^{-1}}$ at its maximum, while the surface velocity is typically greater than $1\,\mathrm{m\,s^{-1}}$: the Eulerian distortion, driven by the effective advection velocity, is therefore smaller than the Lagrangian distortion, driven by the difference between this effective advection and the surface velocity transporting the drifter.

For small scale internal tides on the other hand, ray theory can be used to describe their propagation through the background flow (Broutman et al. 2004). This approach shows that wave packets are advected by the local flow, which is associated with a Doppler shifting of the Eulerian frequency: $\omega = \hat{\omega} + \mathbf{k} \cdot \mathbf{U}$, where $\omega$ and $\hat{\omega}$ are respectively the tide absolute (or Eulerian) and intrinsic (as measured in a frame of reference moving with the balanced flow) frequencies and $\mathbf{k}$ is the wave vector. Ignoring advection of the drifter by the tidal current, the signal measured by the drifter coincides with the tidal field in the frame co-moving with the mean flow with least distortion in the Lagrangian frame of reference. This situation is opposite to the configuration investigated here, as Lagrangian autocorrelation exhibits faster decrease with time lag compared to Eulerian auto-correlation, and the theoretical model proposed here would obviously not be relevant.

In a realistic configuration, the range of validity of each of these two regimes (e.g. small vs large scale internal tide) remains to be quantified.

*b. On the internal tide spatial incoherence*

Another assumption of the theoretical model required to derive (16) is that spatial variations of the complex tidal amplitude may be neglected. In reality the amplitude of the internal tide propagates with the internal tide group speed, which results in spatial variabil-

ity if a temporal one is admitted. A reasonable estimate of the associated horizontal length scale is $\tilde{T}_E c_g$. A sufficient condition for (16) to hold is thus that the drifter displacement after a decorrelation time scale $\tilde{T}_L$ remains smaller than the complex amplitude horizontal length scale:

$$\delta X(\tilde{T}_L) \ll \tilde{T}_E c_g. \tag{24}$$

An upper bound for this displacement is $\tilde{T}_L \max(\bar{V}, \tilde{V})$, which enables to rewrite the preceding condition as:

$$\frac{\tilde{T}_L}{\tilde{T}_E} \ll \frac{c_g}{\max(\bar{V}, \tilde{V})}. \tag{25}$$

We believe this condition is met in general based on 1/ typical values for $c_g$ (around $2\,\mathrm{m/s}$ for the first mode semi-diurnal internal tide at mid-latitude (Zhao 2017)) and flow amplitude, 2/ observations that $\tilde{T}_L \leq \tilde{T}_E$, this inequality being self-consistent with theoretical model predictions and 3/ the observation that stronger flows and thus weaker $c_g/\bar{V}$ concur with smaller $\tilde{T}_L/\tilde{T}_E$ ratios.

Spatial inhomogeneities of the tidal amplitude could, at the cost of added complexity, potentially be included in the model without the approximation (16). This would require combining information about horizontal displacement distribution and the tidal amplitude spatial-temporal autocorrelation. However, diagnostics of spatio-temporal autocorrelation of the internal tide field have never been reported – to our knowledge.

### *c. Autocorrelation models and coherent/incoherent decomposition*

Heuristic choices have been made regarding the shape of the internal tide and balanced motion autocorrelation. Limits to these choices are visible on Figure 4c for balanced motions and are speculated to affect estimates of internal tide incoherent time scales in the southern part of the domain.

At earlier stage of this work, we chose an envelope for the internal tide autocorrelation that included a single exponential decaying term instead of the sum of coherent/incoherent

contributions. We eventually abandoned this choice, because it does not naturally lead to a decomposition of the signal into coherent/non-coherent contributions, and because it resulted in overly large time scales in coherent cases (>1000 days). One may also fit the more general form Eq.(23) to Lagrangian autocorrelations, for example, and evaluate its relevance compared to the single linear exponential form. This would add one more parameter to estimate, however, and would require to determine whether this more general form leads to a significant an improvement which we felt was a study on its own. Therefore, we did not attempt to do this in favour of a more qualitative assessment of the theory.

Determining what form is more appropriate for Eulerian/Lagrangian low-frequency/internal tide autocorrelations is a study on its own that will require more advanced statistical tools (Sykulski et al. 2016; Gurarie et al. 2017) and that we believe may be more relevant to perform in realistic settings (e.g. observation or numerical simulations). Sykulski et al. (2016) proposes a more general alternative with the Matérn process which may help to more accurately modeling statistically the low frequency signal.

## 6. Conclusion

This study investigated, in idealized numerical simulations, the signature of internal tides on surface velocities via the computation of averaged autocorrelations and fits of these autocorrelations on heuristic models. This exercise was performed on both Eulerian and Lagrangian time series which enabled to compare and contrast internal tide signatures in both frames of reference. The central result of this study is that displacements of drifters induced by low-frequency motions produce distortions of the tide signals in Lagrangian time series which results in larger levels of incoherence compared to Eulerian ones. We coined this process "apparent incoherence". Sensitivity experiments enabled to verify that this apparent incoherence is increasing with balanced-motion intensity. A theoretical

model, relating Lagrangian averaged autocovariances to Eulerian ones and accounting for apparent incoherence, was derived and validated against observed estimates.

These results highlight the relevance of GDP data for the mapping of global internal tide properties. More specifically, we were able to recover the total internal tide variance from drifter velocity averaged autocorrelations. Pending validation in more realistic conditions, the knowledge of the distribution of internal tide surface kinetic energy that could be inferred from drifter tracks would be a substantial constraint for the mapping of internal tides. Our study suggests that the identification of (Eulerian) coherent versus incoherent contributions from drifter data may be complicated because of apparent incoherence, as anticipated in earlier studies (Zaron and Elipot 2020). This may still be feasible in areas where incoherence is significant and rapid and/or where low-frequency variability is weak. The theoretical model developed may provide guidance in order to decide where this may occur in the ocean.

Improved mapping of internal tides are directly relevant to the future analysis of SWOT data, to the validation of emerging high resolution global numerical simulations resolving tides (Arbic et al. 2018; Yu et al. 2019), as well as to our fundamental understanding of internal tide lifecycle.

More advanced and likely efficient statistical tools may be required before tackling realistic configurations. Substantial difficulties are associated with the superposition of motions in the real ocean (neighboring tidal harmonics, near-inertial variability) and with the effective statistical stationarity of these motions. Parametric estimations based on maximum likelihood theory offer promising perspectives whether formulated in spectral space (Sykulski et al. 2019) or temporal space (Fleming et al. 2014). Filtering based approaches taking into account the bivariate nature of the velocity signal may also be relevant Lilly and Olhede (2009). These tools may help identify which statistical models are better suited to describe tidal and low-frequency variability as well as resolve the

temporal evolution of the parameters (e.g. amplitude, frequency, bandwidths) describing these processes, which would be a substantial improvement over descriptions of the averaged variability.

The estimation of internal tides properties in a realistic set-up will be carried out using MITgcm simulation LLC4320 using Eulerian outputs of the simulation as well as Lagrangian simulated trajectories. Further analysis should enable us to estimate if our results hold in realistic configuration.

## References


Arbic, B. K., and Coauthors, 2018: Primer on global internal tide and internal gravity wave continuum modeling in hycom and mitgcm. *New frontiers in operational oceanography*, 307–392.

Broutman, D., J. W. Rottman, and S. D. Eckermann, 2004: Ray Methods for Internal Waves in the Atmosphere and Ocean. *JGR*.

Buijsman, M. C., B. K. Arbic, J. G. Richman, J. F. Shriver, A. J. Wallcraft, and L. Zamudio, 2017: Semidiurnal internal tide incoherence in the equatorial p acific. *Journal of Geophysical Research: Oceans*, **122 (7)**, 5286–5305.

Chelton, D. B., M. G. Schlax, R. M. Samelson, J. T. Farrar, M. J. Molemaker, J. C. McWilliams, and J. Gula, 2019: Prospects for future satellite estimation of small-scale variability of ocean surface velocity and vorticity. *Progress in Oceanography*, **173**, 256–350.

Chen, G., and Coauthors, 2019: Concept design of the "guanlan" science mission: China's novel contribution to space oceanography. *Frontiers in Marine Science*, **6**, 194.

Davis, R., 1983: Oceanic property transport, lagrangian particle statistics, and their prediction. *Journal of Marine Research*, **41 (1)**, 163–194.

Davis, R. E., 1985: Drifter observations of coastal surface currents during CODE: The method and descriptive view. *J. Geophys. Res.*, **90(C3)**, 4741–4755.

Duda, T. F., Y.-T. Lin, M. Buijsman, and A. E. Newhall, 2018: Internal Tidal Modal Ray Refraction and Energy Ducting in Baroclinic Gulf Stream Currents. *JPO*, **48 (9)**, 1969–1993, doi:10.1175/JPO-D-18-0031.1.

Dunphy, M., A. L. Ponte, P. Klein, and S. Le Gentil, 2017: Low-mode internal tide propagation in a turbulent eddy field. *Journal of Physical Oceanography*, **47 (3)**, 649–665.

Efron, B., 1981: Censored data and the bootstrap. *Journal of the American Statistical Association*, **76 (374)**, 312–319.

Elipot, S., R. Lumpkin, R. C. Perez, J. M. Lilly, J. J. Early, and A. M. Sykulski, 2016: A global surface drifter data set at hourly resolution. *Journal of Geophysical Research: Oceans*, **121 (5)**, 2937–2966.

Elipot, S., R. Lumpkin, and G. Prieto, 2010: Modification of inertial oscillations by the mesoscale eddy field. *Journal of Geophysical Research: Oceans*, **115 (C9)**.

Fleming, C. H., J. M. Calabrese, T. Mueller, K. A. Olson, P. Leimgruber, and W. F. Fagan, 2014: Non-markovian maximum likelihood estimation of autocorrelated movement processes. *Methods in Ecology and Evolution*, **5 (5)**, 462–472.

Garrett, C., and E. Kunze, 2007: Internal tide generation in the deep ocean. *Annu. Rev. Fluid Mech.*, **39**, 57–87.

Gurarie, E., C. H. Fleming, W. F. Fagan, K. L. Laidre, J. Hernández-Pliego, and O. Ovaskainen, 2017: Correlated velocity models as a fundamental unit of animal movement: Synthesis and applications. *Movement Ecology*, **5 (1)**, 13, doi: 10.1186/s40462-017-0103-3.

Jones, E., T. Oliphant, P. Peterson, and Coauthors, 2001–: SciPy: Open source scientific tools for Python: Least square regression. [Available online at https://docs.scipy.org/doc/scipy/reference/generated/scipy.optimize.curve_fit.html].

Kelly, S. M., and P. F. J. Lermusiaux, 2016: Internal-tide interactions with the Gulf Stream and Middle Atlantic Bight shelfbreak front. *JGR*, **121 (8)**, 6271–6294, doi: 10.1002/2016JC011639.

LaCasce, J., 2008: Statistics from lagrangian observations. *Progress in Oceanography*, **77 (1)**, 1–29.

Lilly, J. M., and S. C. Olhede, 2009: Bivariate instantaneous frequency and bandwidth. *IEEE Transactions on Signal Processing*, **58 (2)**, 591–603.

Lumpkin, R., A.-M. Treguier, and K. Speer, 2002: Lagrangian eddy scales in the northern atlantic ocean. *Journal of physical oceanography*, **32 (9)**, 2425–2440.

Middleton, J. F., 1985: Drifter spectra and diffusivities. *Journal of Marine Research*, **43 (1)**, 37–55.

Morrow, R., and Coauthors, 2019: Global observations of fine-scale ocean surface topography with the surface water and ocean topography (swot) mission. *Frontiers in Marine Science*, **6**, 232.

Nelson, A. D., B. K. Arbic, E. D. Zaron, A. C. Savage, J. G. Richman, M. C. Buijsman, and J. F. Shriver, 2019: Toward realistic nonstationarity of semidiurnal baroclinic tides in a hydrodynamic model. *Journal of Geophysical Research: Oceans*, **124 (9)**, 6632–6642.

Ponte, A. L., and P. Klein, 2015: Incoherent signature of internal tides on sea level in idealized numerical simulations. *Geophysical Research Letters*, **42 (5)**, 1520–1526.

Ponte, A. L., P. Klein, M. Dunphy, and S. Le Gentil, 2017: Low-mode internal tides and balanced dynamics disentanglement in altimetric observations: Synergy with surface density observations. *Journal of Geophysical Research: Oceans*, **122 (3)**, 2143–2155.

Pope, S. B., 2015: *Turbulent Flows*. Cambridge Univ. Press, 771 pp.

Ray, R. D., and E. D. Zaron, 2016: M2 internal tides and their observed wavenumber spectra from satellite altimetry. *Journal of Physical Oceanography*, **46 (1)**, 3–22.

Savage, A., and Coauthors, 2020: Low-mode internal tides and small scale surface dynamics in the swot cal/val region. *Ocean Sciences Meeting 2020*, AGU.

Savva, M. A., and J. Vanneste, 2018: Scattering of internal tides by barotropic quasi-geostrophic flows. *Journal of Fluid Mechanics*, **856**, 504–530.

Sykulski, A. M., S. C. Olhede, A. P. Guillaumin, J. M. Lilly, and J. J. Early, 2019: The debiased Whittle likelihood. *Biometrika*, **106 (2)**, 251–266, doi:10.1093/biomet/asy071, URL https://doi.org/10.1093/biomet/asy071.

Sykulski, A. M., S. C. Olhede, J. M. Lilly, and E. Danioux, 2016: Lagrangian time series models for ocean surface drifter trajectories. *Journal of the Royal Statistical Society: Series C (Applied Statistics)*, **65 (1)**, 29–50.

Veneziani, M., A. Griffa, A. M. Reynolds, and A. J. Mariano, 2004: Oceanic turbulence and stochastic models from subsurface lagrangian data for the northwest atlantic ocean. *Journal of physical oceanography*, **34 (8)**, 1884–1906.

Wagner, G., and W. Young, 2015: Available potential vorticity and wave-averaged quasi-geostrophic flow. *Journal of Fluid Mechanics*, **785**, 401–424.

Wang, J., L.-L. Fu, H. S. Torres, S. Chen, B. Qiu, and D. Menemenlis, 2019: On the spatial scales to be resolved by the surface water and ocean topography ka-band radar interferometer. *Journal of Atmospheric and Oceanic Technology*, **36 (1)**, 87–99.

Whalen, C. B., C. de Lavergne, A. C. N. Garabato, J. M. Klymak, J. A. Mackinnon, and K. L. Sheen, 2020: Internal wave-driven mixing: governing processes and consequences for climate. *Nature Reviews Earth & Environment*, **1 (11)**, 606–621.

Yu, X., A. L. Ponte, S. Elipot, D. Menemenlis, E. Zaron, and R. Abernathey, 2019: Surface kinetic energy distributions in the global oceans from a high-resolution numerical model and surface drifter observations. *Geophys. Res. Lett.*

Zaron, E. D., 2017: Mapping the nonstationary internal tide with satellite altimetry. *Journal of Geophysical Research: Oceans*, **122 (1)**, 539–554.

Zaron, E. D., 2019: Baroclinic tidal sea level from exact-repeat mission altimetry. *Journal of Physical Oceanography*, **49 (1)**, 193–210.

Zaron, E. D., and S. Elipot, 2020: An assessment of global ocean barotropic tide models using geodetic mission altimetry and surface drifters. *Journal of Physical Oceanography*.

Zhao, Z., 2017: Propagation of the Semidiurnal Internal Tide: Phase Velocity Versus Group Velocity. *Geophys. Res. Lett.*, **44 (23)**, 11,942–11,950, doi:10.1002/2017GL076008.

Zhao, Z., M. H. Alford, J. B. Girton, L. Rainville, and H. L. Simmons, 2016: Global observations of open-ocean mode-1 m2 internal tides. *Journal of Physical Oceanography*, **46 (6)**, 1657–1684.

## List of Figures

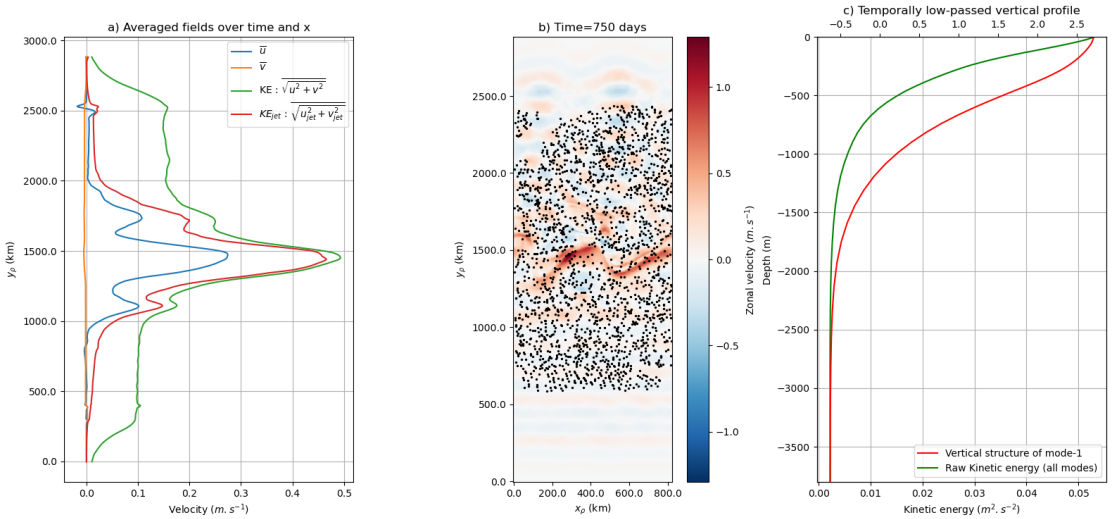


Figure 1. (a) : Mean field of zonal (blue line), meridional (orange line), total (green) and low-passed (red) velocity amplitudes ; (b) : Zonal velocity at t=750 days (color) with positions of 1/4 of the drifters at the same time represented by black dots. (c) : Averaged temporally low-passed kinetic energy and vertical structure of first baroclinic mode at the center of the numerical domain, x≃500km and y≃1450km.

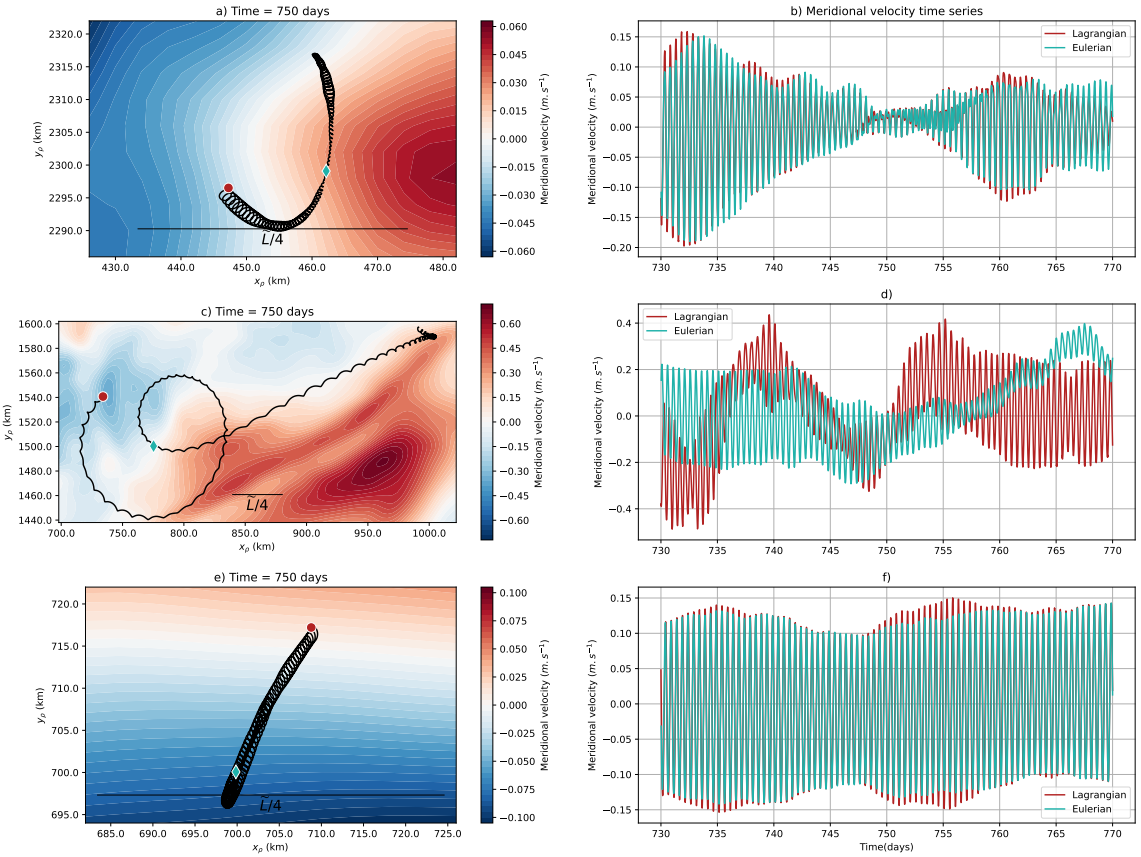


Figure 2. Trajectories of 3 drifters in three different area of the domain (north (a and b), central (c and d) and south (e and f)) over a period of 40 days and corresponding time series. Left column : Trajectory of each the drifter (black line) with the meridional velocity in the background. The red circle represents the position of the drifter at initial time, t0, and the blue diamond the position at mid period. A black straight line is plotted representing a quarter of the wavelength. Right column : Meridional velocity time series along the drifter trajectory in red and at a fixed position (blue diamond in the left figure) in blue.

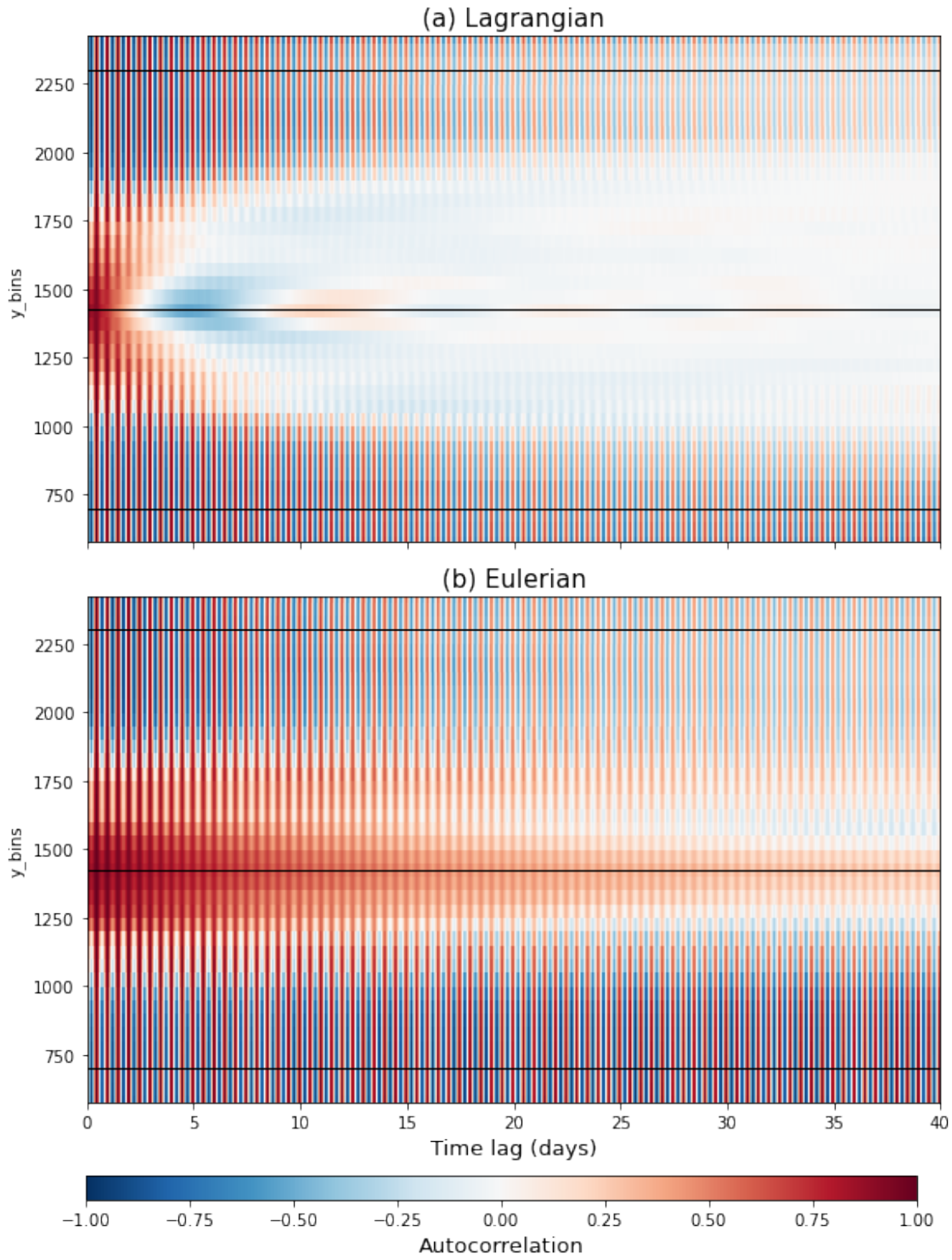


Figure 3. Autocorrelation of meridional velocity v computed from Lagrangian outputs (a) and Eulerian one (b). The y-axis corresponds to the y bins in which the autocorrelation have been averaged. The x-axis is the time lag. Horizontal black lines indicate the three latitudes of interest discussed in the paper (see Figs. 2 and 4)

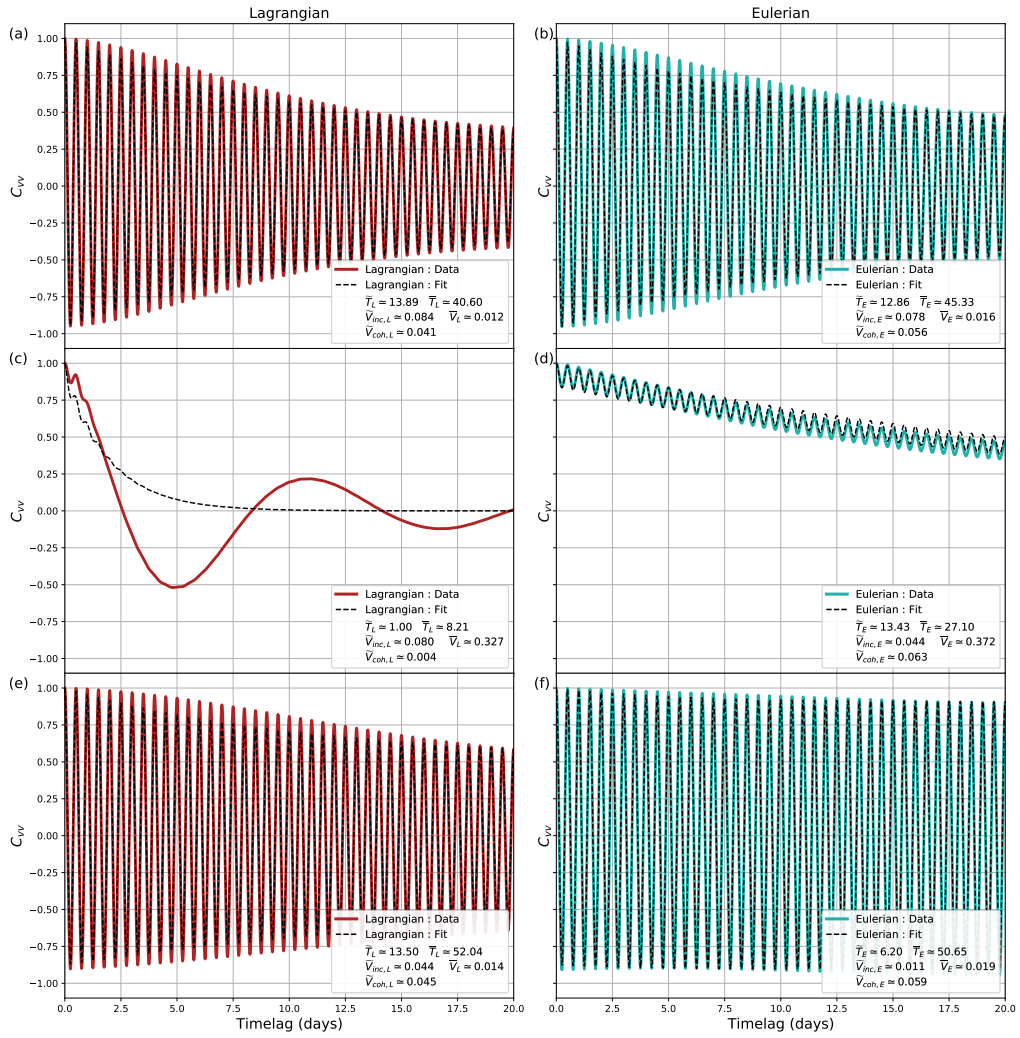


Figure 4. Autocorrelation of meridional velocity at fixed bin in three different area : north (a and b), center (c and d) and south (e and f) of the domain). The Eulerian (right column) and Lagrangian (left column) autocorrelation derived from our data are represented respectively in blue and red. The autocorrelation corresponding to the best fit of our theoretical model (eq.(7)) with the averaged autocovariance are plotted in black dashed lines. Corresponding values of the fitted parameters are indicated in each panel.

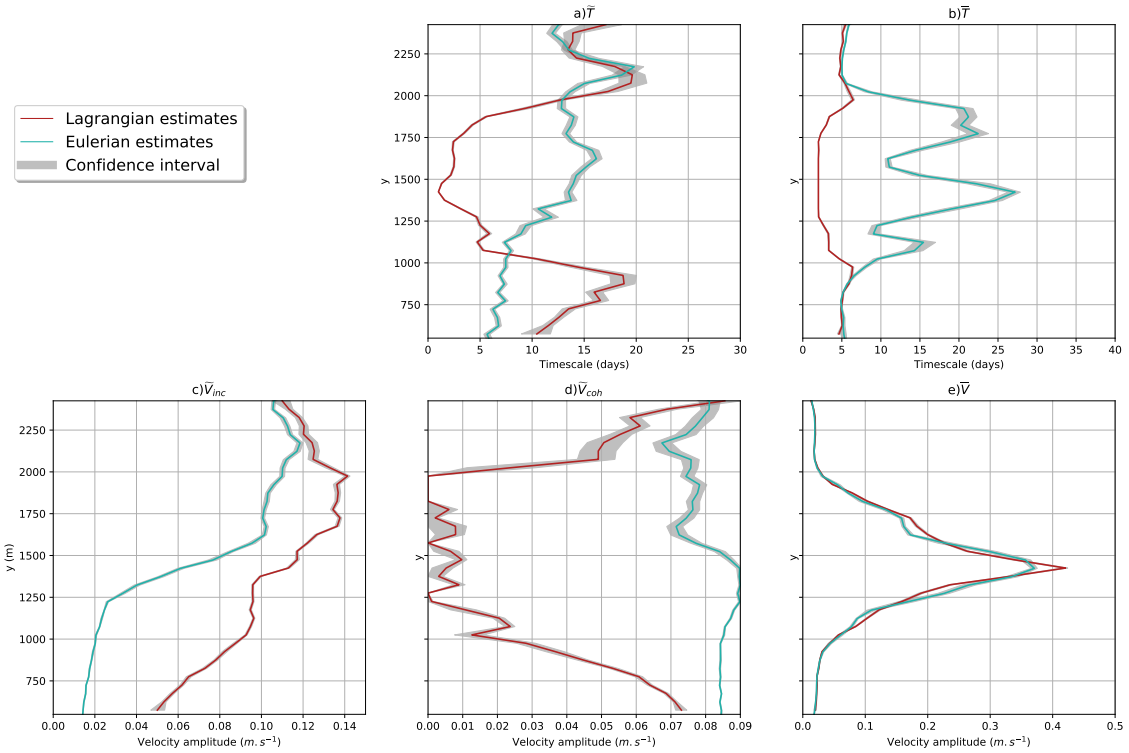


Figure 5. Estimated eulerian (blue lines) and Lagrangian (red lines) incoherence timescale, $\widetilde{T}$ (a), decorrelation of the balanced flow, $\overline{T}$ (b) and tidal and balanced components amplitudes, $\widetilde{V}_{inc}$ (c), $\widetilde{V}_{coh}$ (d) and $\overline{V}$ (e). The estimates are found by fitting the theoretical model (Eq.(10)) to the autocorrelation of v. Error due to sampling are computed via bootstrap and represented by the gray area.

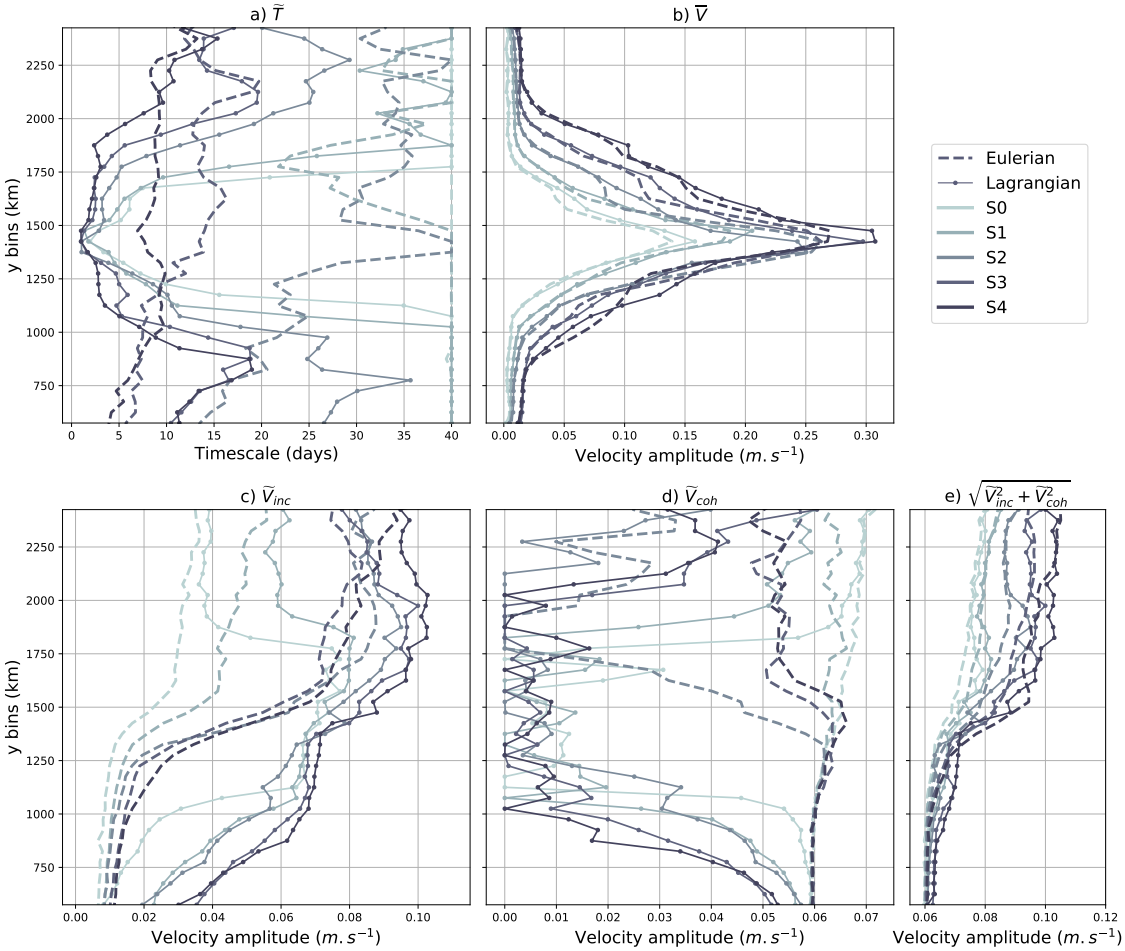


Figure 6. Estimated parameters for five simulations. (a) Lagrangian and Eulerian internal tides incoherence timescales, $\widetilde{T}$. (c), (d) and (e) : Internal tide incoherent and coherent velocity amplitudes, $\widetilde{V}_{inc}$ and $\widetilde{V}_{coh}$ and total tidal amplitude, $\sqrt{\widetilde{V}_{inc}^2 + \widetilde{V}_{coh}^2}$. (b) balanced flow amplitude, $\overline{V}$ is also represented. Incoherence timescales lower than 1 day and larger than 40 days were not allowed by our fitting procedure.

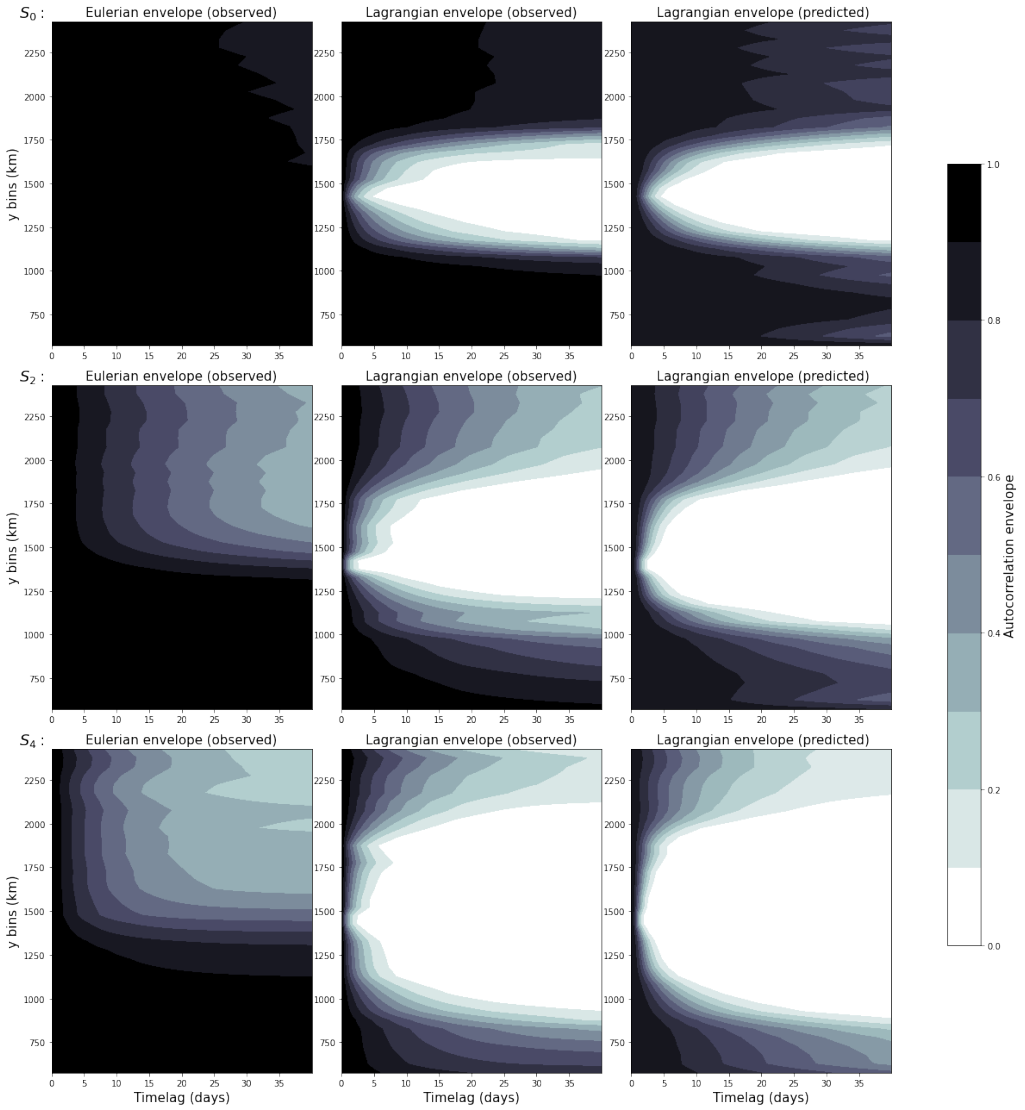


Figure 7. Envelope of the internal tide autocorrelation functions for 3 simulations (corresponding to rows). From top to bottom the balanced flow's strength increases. The envelope of the fitted Eulerian (left column) and Lagrangian (middle column) autocorrelation as well as the predicted Lagrangian autocorrelation (right column) are plotted.

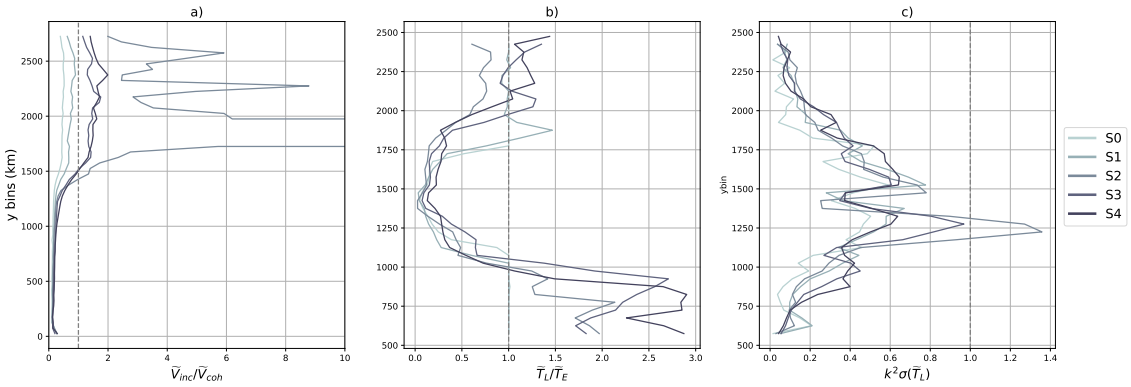


Figure 8. Level of incoherence, ratio of Eulerian incoherent to coherent amplitudes (a) $\widetilde{V}_{inc}/\widetilde{V}_{coh}$ and (b) $r_E = \widetilde{T}_L/\widetilde{T}_E$ as well as (c) the term in the exponential (Eq. (22)), $r_{a,inc} = k^2\sigma^2(\widetilde{T}_L)$, are represented.